Space: Science & Technology
A SCIENCE PARTNER JOURNAL

RESEARCH ARTICLE

Deep Neural Network-Based 4-Quadrant Analog Sun Sensor Calibration

Qinbo Sun[1], Jose Luis Redondo Gutiérrez[2], and Xiaozhou Yu[3]*

[1]School of Astronautics, Northwestern Polytechnical University, Xi'an, China. [2]Institute of Space Systems, German Aerospace Center, Cologne, Germany. [3]Dalian University of Technology, Dalian, China.

*Address correspondence to: yuxiaozhou@dlut.edu.cn

Citation: Sun Q, Gutiérrez JLR, Yu X. Deep Neural Network-Based 4-Quadrant Analog Sun Sensor Calibration. *Space Sci. Technol.* 2023;3:Article 0024. https://doi.org/10.34133/space.0024

Submitted 31 March 2022
Accepted 19 February 2023
Published 27 March 2023

Many error sources influence the calibration experiment of 4-quadrant sun sensors, making the calibration of sun sensors cumbersome and its accuracy difficult to improve. Any continuous function on a bounded closed set can be approximated by a deep neural network. This paper uses the deep neural network model to approximate the error model. The data-driven training network is adopted to continuously modify the model parameters to fit the error compensation model and ensure that the accuracy reaches the target requirements after calibration. Considering that the deep neural network model needs a considerable amount of data, the neural network model training is divided in 2 stages. In the preliminary stage, cubic surface fitting is used to generate a dataset, which is small in size and controllable. After the completion of the initial training, the experimental data are used to fine-tune the model to achieve error compensation. The accuracy can be improved from 1° (1σ) to 0.1° (1σ) after the incident angle of the sun sensor is corrected. The error compensation model eliminates the loss of accuracy caused by the distortion of light spots at the edge of the field angle and provides a favorable condition for the expansion of the field angle of the 4-quadrant analog sun sensor.

Introduction

A spacecraft can estimate the attitude state by comparing external measurements from attitude sensors with reference information. Attitude sensors include Earth sensors, magnetometers, sun sensors, star sensors, etc. With the development of CubeSat technology, sun sensors have played an important part in the CubeSat attitude control system.

Sun sensors, which obtain the attitude information by measuring the sun vector, can be divided into analog and digital sensors. Digital sun sensors generally use changed couple device or charge-coupled device as photosensitive components, with accuracy up to 1″. A 4-quadrant detector or position-sensitive device is used in most analog sun sensors, with an accuracy of 0.15 to 2° [1,2]. Compared with digital sun sensors, analog sun sensors generally have lower accuracy, but have simpler structure and logic, and have advantages in volume, weight, power consumption, and cost [3,4]. CubeSats tend to use analog sun sensors because of the limitation of satellite volume and payload. The 4-quadrant analog solar sensor has the advantages of extremely low power consumption, minimal volume, low complexity, low cost, and high reliability. Various types of sun sensors have been developed and used in satellite missions [5–11].

Researchers have done a lot of analytical modeling work for 4-quadrant analog sun sensors. The Northwestern Polytechnical University [12] and the Delft University of Technology in the Netherlands jointly developed the low-cost micro wireless automatic sun sensor. The sensor implements a 4-quadrant detector as a photosensitive component and has an accuracy of up to 0.5° (1σ), achieved using a 5-order surface fitting equation to calibrate the sensor. However, the calibration experiment only uses the horizontal and vertical points of the photosensitive surface of the solar sensor, without considering assembly errors and spot distortions. Yousefian et al. [13] report the design, fabrication, and error analysis of a sun sensor array composed of 6 photodiodes. The sensor estimates the direction of the sun using a linear least-squares method. The performance of the sensor is deteriorated by 3 major sources: fabrication errors, scattered environmental light, and inexact modeling of photodiodes. Using a calibration procedure and modeling the uniform component of the environmental light, it is possible to mitigate the first 2 errors and importantly reduce the root mean square error from 2.63° to 0.83°. The calibration method involves many error models and requires accurate modeling of a photodiode.

Wang et al. [14] aim to measure errors introduced by assembly deviation. The main error sources (center offset, rotation and tilt between the aperture and silicon cell, and inclination of the optoelectronic component) are analyzed quantitatively, providing the basis for improving the accuracy of the sun sensor. However, the machining error is not analyzed, and the complete compensation method and process are not shown. On the basis of numerical simulation, Xu et al. [15] established and analyzed the influence model of the unconformity in the responsivity of each cell quadrant and the voltage conversion, amplifier, analog-to-digital conversion, and dark current for each quadrant photocurrent. The calibration and compensation of such error sources were proposed, leading to an improvement of the measuring accuracy of the sun sensor from 2.05°

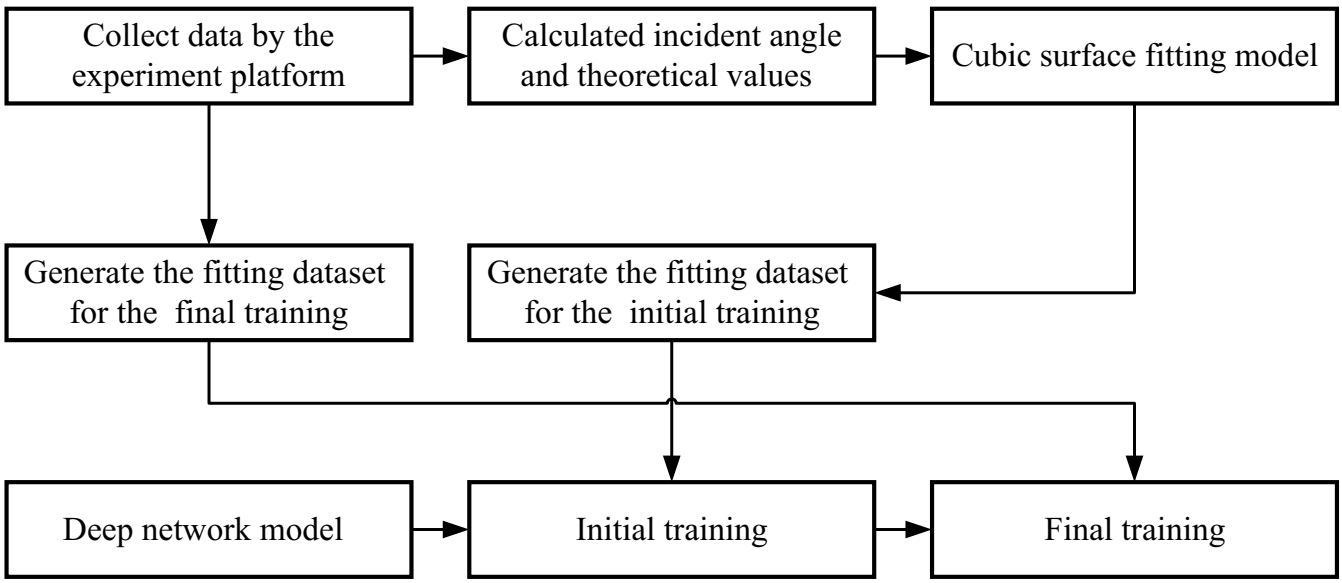

Fig. 1. Calibration experiment flow chart of the sun sensor.

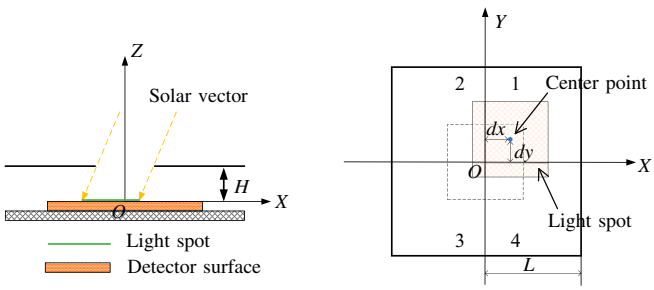

Fig. 2. Working principle of the 4-quadrant detector.

(α axis, 3σ) and 1.94° (β axis, 3σ). However, this method adopts an experimental measurement method in each link of the test process, which requires high precision of the equipment.

Deng et al. [16] proposed a high-precision error compensation method for the 4-quadrant analog sun sensor to improve the accuracy of the micro-nano satellite attitude determination system. The average accuracy before compensation was 3.072° (1σ) within ±40° of the incident angle, and the average accuracy was 0.177° (1σ) after compensation. However, this calibration scheme introduces a considerable number of parameters and has too many kinds of errors to be considered. Adnane et al. [17] present a novel geometry, called 3D shape, of a sun sensor array that contains 3 structures: pyramidal structure in the top, cube structure in the middle, and inverted pyramidal structure in the bottom. The structure aims to increase the field of view (FOV) of the sun sensor by selecting an appropriate tilt angle for the ambient light sensors. This design improves the sun sensor FOV but does not significantly improve its measurement accuracy. Porras Hermoso et al. [18] propose a methodology that allows the calibration and determination of the expected performance of photodiodes in the direct polarization zone for any light spectrum without requiring any specialized equipment. However, this method is used to calibrate the specific response curve of photodiodes. The author does not show the measurement accuracy analysis of the sun sensor.

Fig. 3. Four-quadrant analog sun sensor.

In recent years, artificial intelligence methods, typically represented by deep learning, are widely used in the aerospace field. Deep learning provides new ideas for solving traditional aerospace problems [19–21]. The various error sources affecting the calibration of the 4-quadrant sun sensor lead to a complicated process of compensation model establishment. This paper presents the application of the deep neural network model to fit and approximate the error model of the sun sensor. The data-driven method is adopted to approximate the error compensation model. A deep neural network is a feedforward network with many hidden layers. Universal approximation theorem [22] shows that a feedforward network with a single hidden layer, the simplest form of the multilayer perceptron, containing a finite number of hidden neurons, is a universal

approximator among continuous functions on compact subsets of $\boldsymbol{R}_n$, under mild assumptions on the activation function. Similarly, the derivative of the feedforward network can arbitrarily fit the derivative of the function [23]. This shows that any continuous function on bounded closed sets can be approximated by using neural networks, which provides theoretical support for fitting the error compensation model of the sun sensor with a deep neural network.

On the basis of the universal approximation theorem, this paper proposes a method to calibrate sun sensors by deep learning, which not only is able to integrate the influence of various errors but also avoids the need of analyzing and modeling every single error. The training of a deep neural network model requires a large amount of data, as the network cannot converge when the dataset is not large enough. On the other hand, the measurement data size is limited by the calibration experiment. Therefore, the neural network model training is divided into 2 stages. The process is shown in Fig. 1. In the first stage, the sun sensor cubic surface fitting model was used to generate a simulated dataset, and the size of the dataset could be specified.

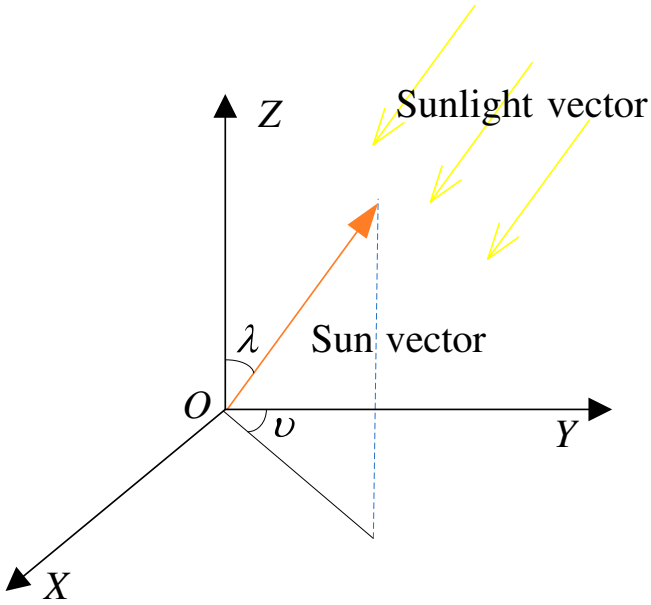

Fig. 4. Solar ray vector angle diagram.

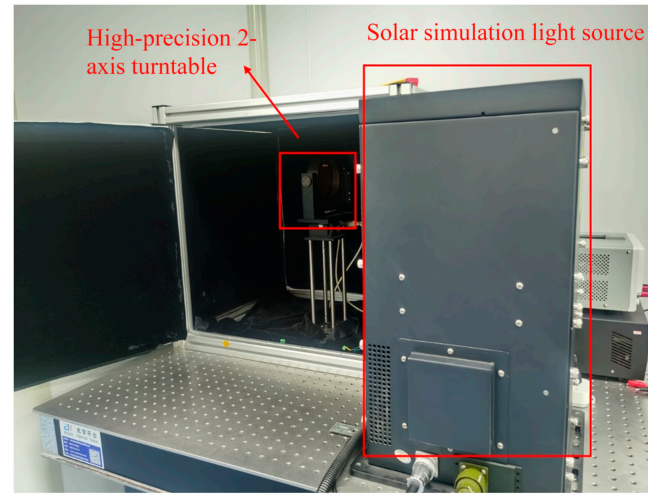

Fig. 5. The calibration and testing platform of the sun sensor.

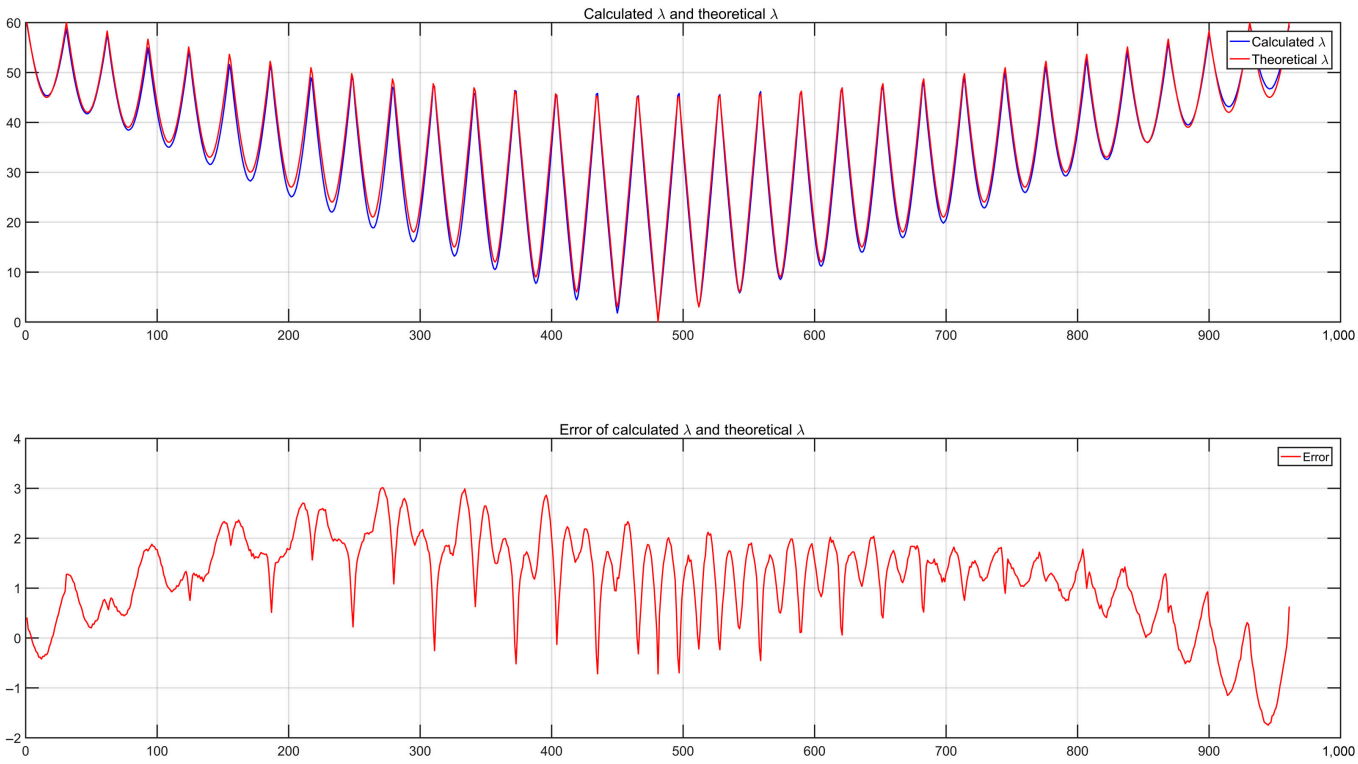

Fig. 6. The calculated incident angle is compared with the theoretical value.

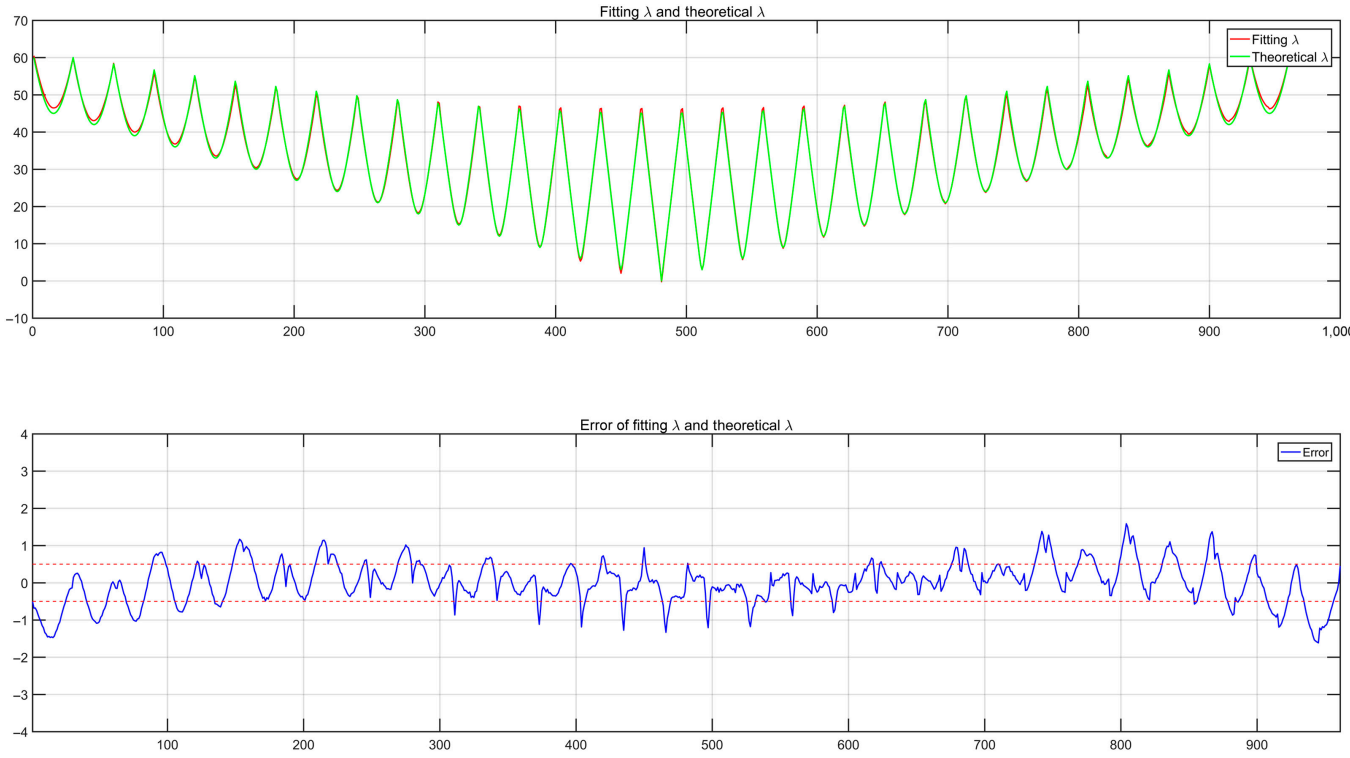

Fig. 7. Fitting value and actual value of incident angle.

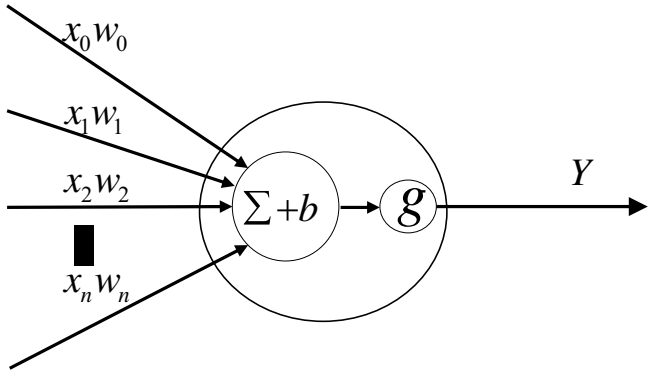

Fig. 8. The simplest neuron structure.

Table 1. Incidence parameters.

Parameter	Value	Parameter	Value
q_{00}	2.7277	q_{10}	−0.5326
q_{01}	1.1320	q_{20}	0.7169
q_{11}	0.1975	q_{02}	−0.7268
q_{30}	0.0692	q_{21}	−0.2623
q_{12}	−0.0076	q_{03}	0.0791

The neural network model is trained with this simulated dataset. In the following stage, the actual measurement data are used to fine-tune the model to approximate the actual error model. The incident angle accuracy of the sun sensor is 1° (1σ) before correction. After the correction of the neural network model, the accuracy is improved to 0.1° (1σ).

The remainder of this paper is organized as follows. The "Principle of 4-quadrant analog sun sensor" section introduces the principle of the four-quadrant analog sun sensor. The "Cubic surface fitting" section explains the calibration process of sun sensor based on cubic surface fitting. In the "Deep network model" section, the algorithm of the training network is introduced. In the "Deep network model training and result analysis" section, the performance of the proposed algorithm is verified using experimental data. Finally, the conclusions are summarized in the "Conclusion" section.

Principle of 4-Quadrant Analog Sun Sensor

The sun sensor can measure the vector direction of the solar rays, which can be used to determine the attitude of the spacecraft. The output of analog sun sensors is an analog signal, current, or voltage. The incident angle and azimuth angle of the solar ray vector on the satellite surface will be different when the satellite is in a different attitude. The sun sensor used in the integrated attitude measurement unit system is an analog one based on the 4-quadrant detector.

The 4-quadrant detector contains 4 square photodiodes with side length L. The performance of the 4 photodiodes is identical. The photodiodes are arranged in a 4-quadrant system and combined into a photoelectric detection array. To analyze the solar vector information, a 2-dimensional rectangular coordinate system XOY can be established on the surface of the detector, with the center of the photodetector as the origin and the intersection of the 4 photodiodes as the X and Y axes.

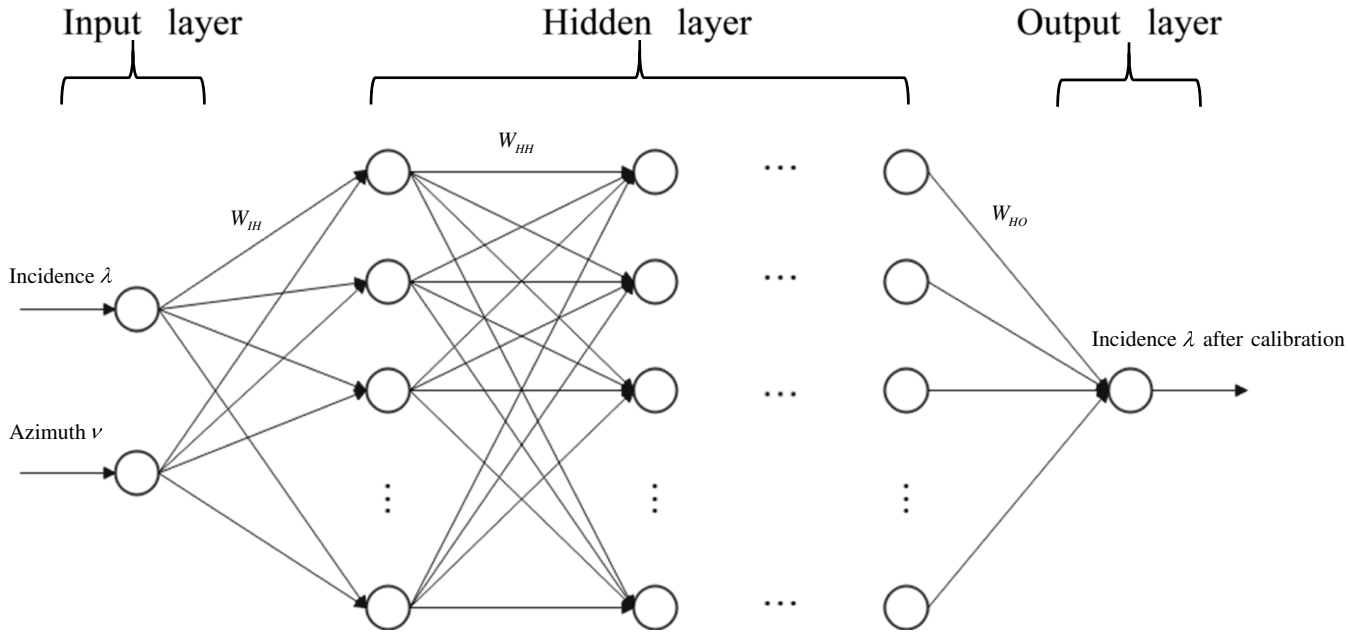

Fig. 9. Deep neural network model.

Table 2. Structural parameters of feedforward neural network.

Parameters	Structure	Details	Parameters	Structure	Details
Layers	Input	1	Activation function	Input	ReLU
	Hidden	6		Hidden	ReLU
	Output	1		Output	Linear
Nodes	Input	2	Learning	-	Adam
	Hidden	35	Training	Epochs	500
	Output	1	-	-	-

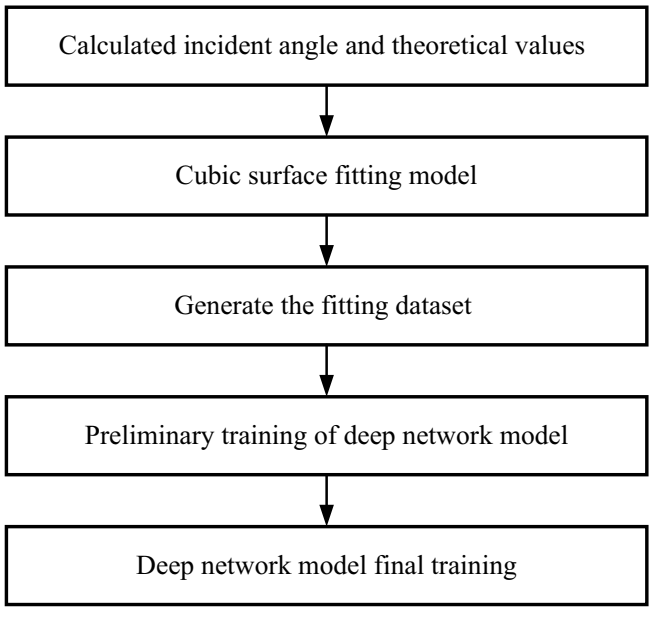

Fig. 10. Generate datasets and model training flow.

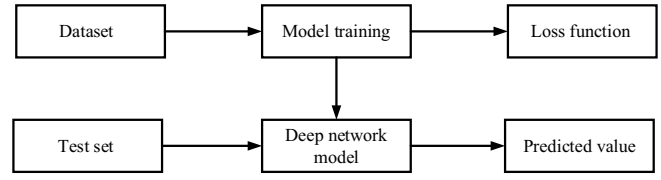

Fig. 11. Schematic diagram of model training and testing.

As shown in Fig. 2, a square light hole is left directly above the detector. The sides of the hole (also of length L) are aligned with the X axis and Y axis, and the center point is adjusted to the perpendicular line of the detector surface passing through the origin O. H is the distance between the light hole and the 4-quadrant detector surface. Through geometric analysis, the FOV of the sun sensor can be obtained as:

$$\mathrm{FOV} = 2\arctan\left(\frac{L}{2H}\right) \tag{1}$$

In the 4-quadrant analog sun sensor, the side length of the photodiode and the side length of light hole $L = 5$ mm, and the distance between the through-light hole and the detector surface $H = 1.4$ mm. The FOV of the sensor can be calculated as ±60°.

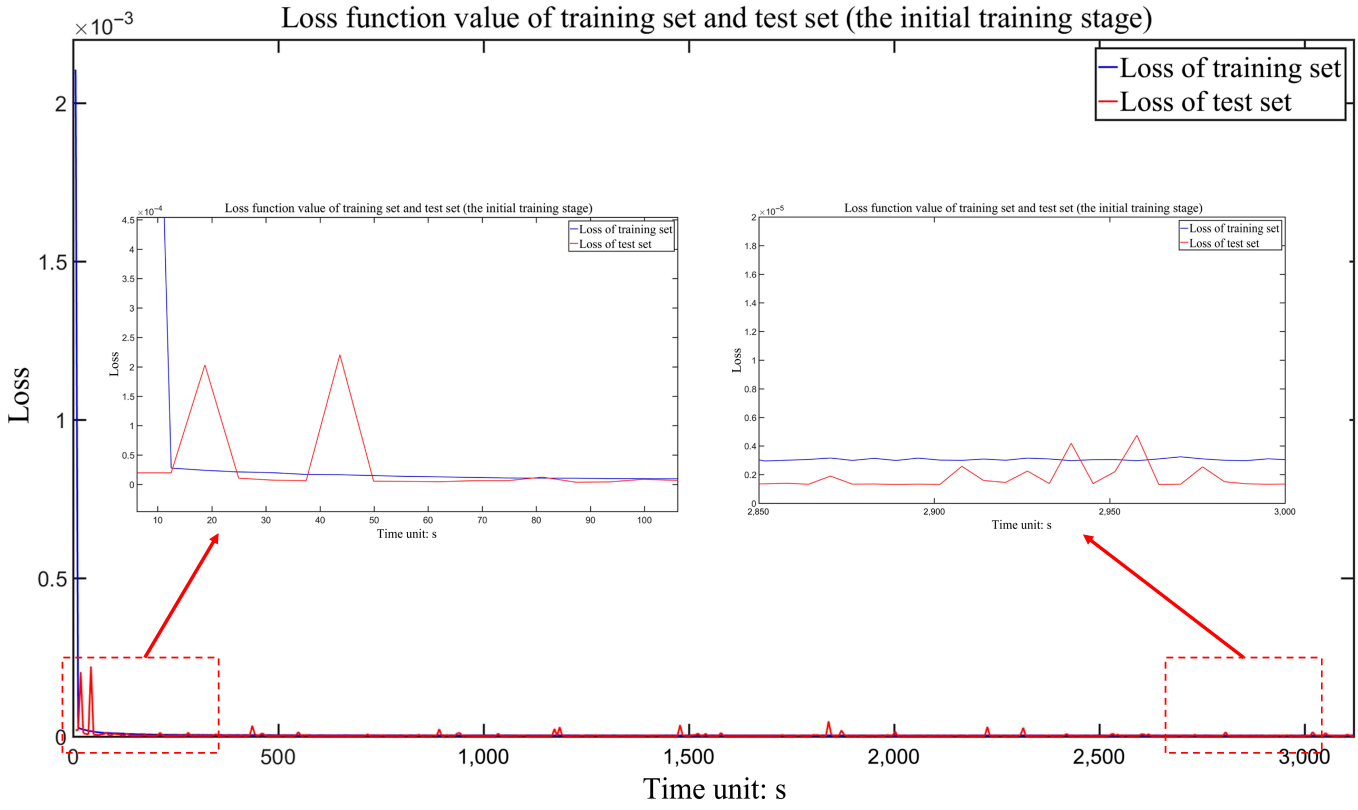

Fig. 12. Training loss of network initial training set and test set.

As shown in Fig. 2, spots will be formed in the 4 quadrants of the detector when the solar ray vector passes through the light hole. The photodiode outputs a 4-way current signal when it is illuminated by light. When the solar ray is not vertically incident, the 4-way output current will also change according to the deviation of the spot center. By analyzing the geometric relationship, the incidence λ and azimuth υ of the solar vector (see Fig. 4) can be expressed as:

$$\lambda = \tan^{-1}\frac{\sqrt{dx^2+dy^2}}{H} \tag{2}$$

$$\upsilon = \begin{cases} \tan^{-1}\dfrac{dy}{dx}, dx>0 \\ 90°, dx=0, dy>0 \\ -90°, dx=0, dy<0 \\ 0°, dx=0, dy=0 \end{cases} \tag{3}$$

where dx and dy are the coordinates of the central point of the spot. The incidence λ is the angle between the incident solar ray and the positive direction of the OZ axis. The azimuth υ is the angle between the projection of the incident solar ray in the XOY plane and the OX axis, which is positive counterclockwise. The 4-quadrant analog sun sensor is shown in Fig. 3.

The 4 photodiodes of the detector have the same nominal performance. The output current of the photodiode is related to the area illuminated on the photodiode (assuming the same light intensity). I_0 is the output current when sunlight illuminates the photodiode completely and from a vertical direction. I_1, I_2, I_3, and I_4 are the output currents of the 4 photodiodes, and S_1, S_2, S_3, and S_4 are the spot areas of the 4 photodiodes. δ represents the angle between the solar incident ray and the surface normal of the 4-quadrant detector. The output current of the 4-quadrant detector is expressed as follows:

$$I = I_0 S_i \cos\delta \tag{4}$$

Through geometric analysis, it can be obtained that the position relation between S_1, S_2, S_3, and S_4 and the spot is:

$$\left.\begin{aligned} S_1 &= \left(\frac{L}{2}+dx\right)\left(\frac{L}{2}+dy\right) \\ S_2 &= \left(\frac{L}{2}-dx\right)\left(\frac{L}{2}+dy\right) \\ S_3 &= \left(\frac{L}{2}-dx\right)\left(\frac{L}{2}-dy\right) \\ S_4 &= \left(\frac{L}{2}+dx\right)\left(\frac{L}{2}-dy\right) \end{aligned}\right\} \tag{5}$$

Therefore, the 4-way current output by the photodiode can be expressed as follows:

$$\left.\begin{aligned} I_1 &= I_0\left(\frac{L}{2}+dx\right)\left(\frac{L}{2}+dy\right)\cos\delta \\ I_2 &= I_0\left(\frac{L}{2}-dx\right)\left(\frac{L}{2}+dy\right)\cos\delta \\ I_3 &= I_0\left(\frac{L}{2}-dx\right)\left(\frac{L}{2}-dy\right)\cos\delta \\ I_4 &= I_0\left(\frac{L}{2}+dx\right)\left(\frac{L}{2}-dy\right)\cos\delta \end{aligned}\right\} \tag{6}$$

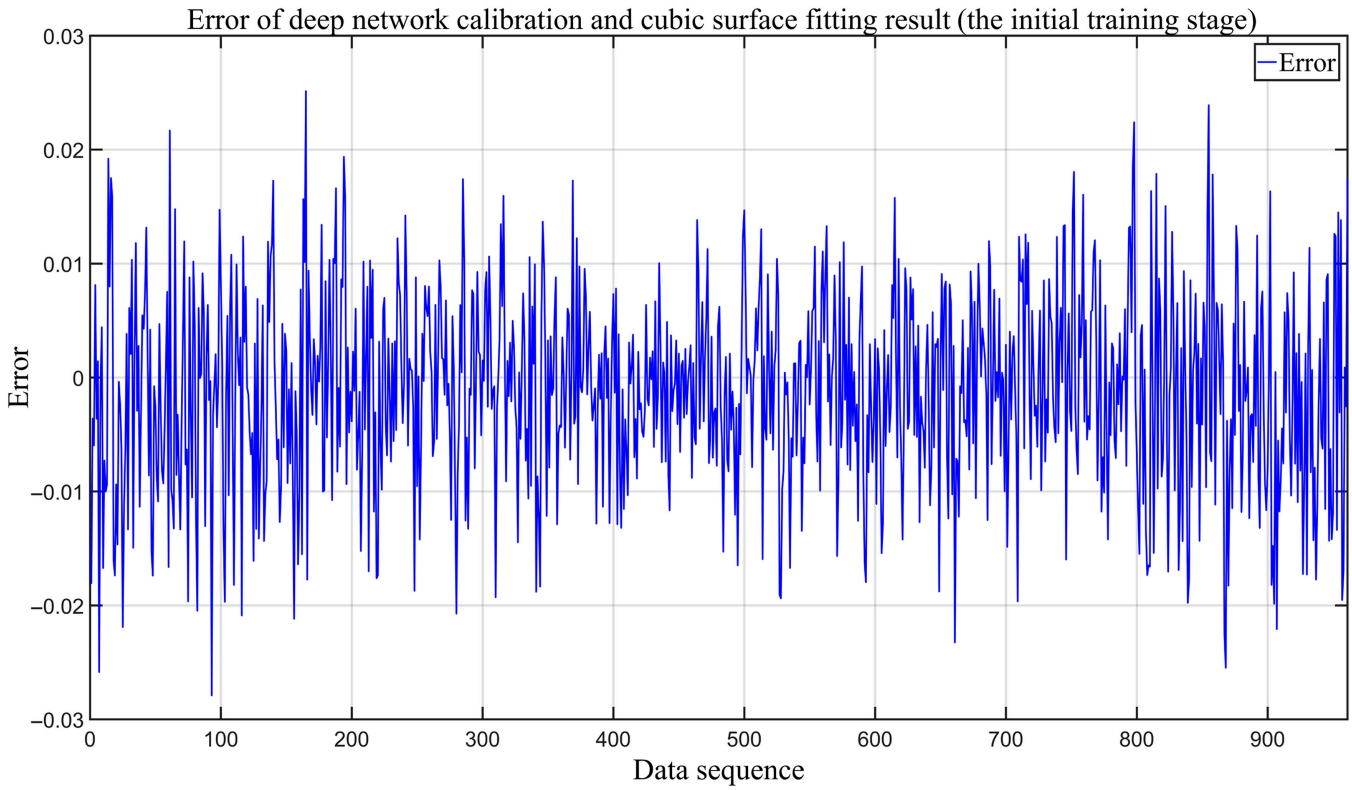

Fig. 13. Error of deep network calibration and cubic surface fitting result.

The coordinates of the center of the illuminated area can be expressed as:

$$\left.\begin{aligned} dx &= \frac{L}{2} \times \frac{I_1 - I_2 - I_3 + I_4}{I_1 + I_2 + I_3 + I_4} \\ dy &= \frac{L}{2} \times \frac{I_1 + I_2 - I_3 - I_4}{I_1 + I_2 + I_3 + I_4} \end{aligned}\right\} \tag{7}$$

The 4-quadrant detector outputs the current signal. To enable the system to collect signals, the current signal needs to be converted into a voltage signal. In this paper, the method of access sampling resistance is used for signal conversion, one end of the resistance is connected to the current output end and the other end is connected to the ground. The operational amplifier circuit amplifies the voltage signal at the current output. The output voltage of the amplifier can reflect the photocurrent by connecting the digital–analog converter. Therefore, the coordinate of the central point of the spot can be expressed as:

$$\left.\begin{aligned} dx &= \frac{L}{2} \times \frac{U_1 - U_2 - U_3 + U_4}{U_1 + U_2 + U_3 + U_4} \\ dy &= \frac{L}{2} \times \frac{U_1 + U_2 - U_3 - U_4}{U_1 + U_2 + U_3 + U_4} \end{aligned}\right\} \tag{8}$$

Cubic Surface Fitting

As shown in Fig. 5, the calibration and testing platform of the sun sensor includes a solar simulation light source, high-precision 2-axis turntable, and servo controller. The solar simulation light source is a space steady-state solar simulator satisfying the AM0 index. The control accuracy of the turntable is less than 0.001°.

In the experiment of data measurement, a high-precision 2-axis turntable with a step length of 3° rotates along with the horizontal and vertical directions of the photosensitive plane of the sun sensor within the whole FOV of the sun sensor. The theoretical values of solar ray incidence λ and azimuth υ at each attitude test point can be obtained from the angle of the turntable. The solar simulator and biaxial turntable were used for data acquisition, and preliminary calculations and error analysis were carried out to analyze the results.

From the test results, there are large errors in the calculation, up to 3°. These errors have a direct effect in the attitude determination. Therefore, calibration experiments are necessary to eliminate errors.

To calibrate the analog sun sensor, a surface fitting scheme is adopted to process the measured data to fit the relationship between the solar vector information measured by the sun sensor and the actual value. The sun sensor surface fitting formula is [24]:

$$\left.\begin{aligned} \lambda &= \sum_{j=0}^{s-i} \sum_{i=0}^{s} p_{ij} v_r^i \lambda_r^j \\ v &= \sum_{j=0}^{s-i} \sum_{i=0}^{s} q_{ij} v_r^i \lambda_r^j \end{aligned}\right\} \tag{9}$$

p_{ij} and q_{ij} are related to the performance of the sun sensor. v_r and λ_r are the actual values of the azimuth and incidence of the sun vector. s is the parameter defining the order of the fitting polynomial. v and λ are the output value of the sun sensor. In this paper, the value of s is 3.

Extending the previous equation, it can be shown that:

$$\left.\begin{aligned} MA &= U \\ MB &= V \end{aligned}\right\} \tag{10}$$

where

$$A=\begin{bmatrix} q_{00} \\ q_{10} \\ q_{01} \\ q_{20} \\ q_{11} \\ q_{02} \\ q_{30} \\ q_{21} \\ q_{12} \\ q_{03} \end{bmatrix}, B=\begin{bmatrix} p_{00} \\ p_{10} \\ p_{01} \\ p_{20} \\ p_{11} \\ p_{02} \\ p_{30} \\ p_{21} \\ p_{12} \\ p_{03} \end{bmatrix}, U=\begin{bmatrix} \sum \nu \\ \sum \nu\nu_r \\ \sum \nu\lambda_r \\ \sum \nu\nu_r^2 \\ \sum \nu\nu_r\lambda_r \\ \sum \nu\lambda_r^2 \\ \sum \nu\nu_r^3 \\ \sum \nu\nu_r^2\lambda_r \\ \sum \nu\nu_r\lambda_r^2 \\ \sum \nu\lambda_r^3 \end{bmatrix}, V=\begin{bmatrix} \sum \lambda \\ \sum \lambda\nu_r \\ \sum \lambda\lambda_r \\ \sum \lambda\nu_r^2 \\ \sum \lambda\nu_r\lambda_r \\ \sum \lambda\lambda_r^2 \\ \sum \lambda\nu_r^3 \\ \sum \lambda\nu_r^2\lambda_r \\ \sum \lambda\nu_r\lambda_r^2 \\ \sum \lambda\lambda_r^3 \end{bmatrix}$$

$$M=\begin{bmatrix} n & \sum \nu_r & \sum \lambda_r & \sum \nu_r^2 & \sum \nu_r\lambda_r & \sum \lambda_r^2 & \sum \nu_r^3 & \sum \nu_r^2\lambda_r & \sum \nu_r\lambda_r^2 & \sum \lambda_r^3 \\ \sum \nu_r & \sum \nu_r^2 & \sum \nu_r\lambda_r & \sum \nu_r^3 & \sum \nu_r^2\lambda_r & \sum \nu_r\lambda_r^2 & \sum \nu_r^4 & \sum \nu_r^3\lambda_r & \sum \nu_r^2\lambda_r^2 & \sum \nu_r\lambda_r^3 \\ \sum \lambda_r & \sum \nu_r\lambda_r & \sum \lambda_r^2 & \sum \nu_r^2\lambda_r & \sum \nu_r\lambda_r^2 & \sum \lambda_r^3 & \sum \nu_r^3\lambda_r & \sum \nu_r^2\lambda_r^2 & \sum \nu_r\lambda_r^3 & \sum \lambda_r^4 \\ \sum \nu_r^2 & \sum \nu_r^3 & \sum \nu_r^2\lambda_r & \sum \nu_r^4 & \sum \nu_r^3\lambda_r & \sum \nu_r^2\lambda_r^2 & \sum \nu_r^5 & \sum \nu_r^4\lambda_r & \sum \nu_r^3\lambda_r^2 & \sum \nu_r^2\lambda_r^3 \\ \sum \nu_r\lambda_r & \sum \nu_r^2\lambda_r & \sum \nu_r\lambda_r^2 & \sum \nu_r^3\lambda_r & \sum \nu_r^2\lambda_r^2 & \sum \nu_r\lambda_r^3 & \sum \nu_r^4\lambda_r & \sum \nu_r^3\lambda_r^2 & \sum \nu_r^2\lambda_r^3 & \sum \nu_r\lambda_r^4 \\ \sum \lambda_r^2 & \sum \nu_r\lambda_r^2 & \sum \lambda_r^3 & \sum \nu_r^2\lambda_r^2 & \sum \nu_r\lambda_r^3 & \sum \lambda_r^4 & \sum \nu_r^3\lambda_r^2 & \sum \nu_r^2\lambda_r^3 & \sum \nu_r\lambda_r^4 & \sum \lambda_r^5 \\ \sum \nu_r^3 & \sum \nu_r^4 & \sum \nu_r^3\lambda_r & \sum \nu_r^5 & \sum \nu_r^4\lambda_r & \sum \nu_r^3\lambda_r^2 & \sum \nu_r^6 & \sum \nu_r^5\lambda_r & \sum \nu_r^4\lambda_r^2 & \sum \nu_r^3\lambda_r^3 \\ \sum \nu_r^2\lambda_r & \sum \nu_r^3\lambda_r & \sum \nu_r^2\lambda_r^2 & \sum \nu_r^4\lambda_r & \sum \nu_r^3\lambda_r^2 & \sum \nu_r^2\lambda_r^3 & \sum \nu_r^5\lambda_r & \sum \nu_r^4\lambda_r^2 & \sum \nu_r^3\lambda_r^3 & \sum \nu_r^2\lambda_r^4 \\ \sum \nu_r\lambda_r^2 & \sum \nu_r^2\lambda_r^2 & \sum \nu_r\lambda_r^3 & \sum \nu_r^3\lambda_r^2 & \sum \nu_r^2\lambda_r^3 & \sum \nu_r\lambda_r^4 & \sum \nu_r^4\lambda_r^2 & \sum \nu_r^3\lambda_r^3 & \sum \nu_r^2\lambda_r^4 & \sum \nu_r\lambda_r^5 \\ \sum \lambda_r^3 & \sum \nu_r\lambda_r^3 & \sum \lambda_r^4 & \sum \nu_r^2\lambda_r^3 & \sum \nu_r\lambda_r^4 & \sum \lambda_r^5 & \sum \nu_r^3\lambda_r^3 & \sum \nu_r^2\lambda_r^4 & \sum \nu_r\lambda_r^5 & \sum \lambda_r^6 \end{bmatrix}$$

Inverting this expression leads to:

$$\begin{bmatrix} A \\ B \end{bmatrix} = \left(M^T M\right)^{-1} M^T \begin{bmatrix} U \\ V \end{bmatrix} \tag{11}$$

The measured data and theoretical values of the analog sun sensor are then substituted into the model. The final parameters are shown in Table 1.

The output value of the analog sun sensor is corrected by the cubic surface fitting model, and the result is seen in Fig. 7.

From the fitting results, it can be concluded that the error is effectively reduced. However, when the spot is close to the edge of the 4-quadrant solar cell, the spot distortion and the limit of the FOV lead to a larger error. This is due to uneven illumination near the edge of the FOV, which is related to the mechanical structure of the sun sensor. Therefore, to analyze the error model, it is necessary to establish a structural model and analyze the mechanical error, which is a cumbersome process.

Deep Network Model

There are many error sources in analog sun sensors, which bring difficulties to the establishment of an error model. Therefore, a deep neural network model is adopted to fit the error correction model, which is able not only to improve the precision of the sensor but also to avoid tedious modeling work. The deep neural network model adopts data-driven learning and training. After learning and training, the deep neural network model approximates the actual error model, which is used for error correction.

Deep feedforward neural network

Deep feedforward neural network is a kind of neural network model with feedforward characteristics. The most representative example of a feedforward neural network is the model of multilayer perception. In the calibration experiment of the analog sun sensor, the deep feedforward neural network is selected to fit the error model.

The feedforward neural network model is forward. There is no connection between the output of the model and the model itself, thus no feedback. The basic unit of the artificial neural network is the "neuron," which is usually a nonlinear element with multiple inputs and a single output. A neural network is an error backpropagation multilayer feedforward neural network and adopts an error backpropagation learning algorithm.

Figure 8 shows the simplest neuron structure. The neuron unit implements the function of summing and weighting all inputs and outputs. ω is the weight, which is the parameter of the neuron. For the final output Y to better match the label of X, neural networks usually involve some optimization processes, adjusting the value of the weights. In addition, it is effective to add activation functions to linear models to achieve delinearization. In the sun sensor calibration network model, ReLU (linear rectification function) is selected as the activation function.

$$g(z) = max\{0,z\} \tag{12}$$

After the ReLU function, the output of a neuron unit can be calculated as follows:

$$Y = g\left(\omega^T X + b\right) \tag{13}$$

Full connection and partial connection are the connection modes between 2 adjacent layers in a neural network model. In full connection mode, all units of the current network layer are connected to each unit of the upper network layer. In the case of partial connection, the units in the current layer of the network are only connected to some of the units in the upper layer of the network. The main purpose of using a partial connection is to reduce the number of network parameters. In the calibration experiment of the sun sensor, the parameter scale is not large. Therefore, the deep network model adopts a full connection mode.

The deep neural network model structure is shown in Fig. 9. There is parameter coupling between azimuth angle and incident angle. Therefore, when the incident angle is calibrated, the input layer of the deep neural network model is the output azimuth and incident angle of the sun sensor ($X = [\lambda, \nu]^T$), and the output layer is the incident angle after calibration ($\mathrm{Net}(X_i;\omega)$).

An important aspect of deep neural network design is the selection of the loss function. In essence, the calibration of the sun sensor is a regression problem, which aims at predicting a specific value. The neural network usually has only one output node to solve the regression problem, and the output value of this node is the predicted value. For regression problems, the most commonly used loss function is the mean square error (MSE) loss function,

$$L(\omega) = \frac{1}{N}\sum_{i=1}^{N}\left\|\mathrm{Net}\left(X_i;\omega\right) - \widehat{\lambda}_i\right\| \tag{14}$$

where $\widehat{\lambda}_i$ is the expected value (theoretical value) of the ith sample in a batch and $f(\lambda_i;\omega)$ is the predictive value of the neural

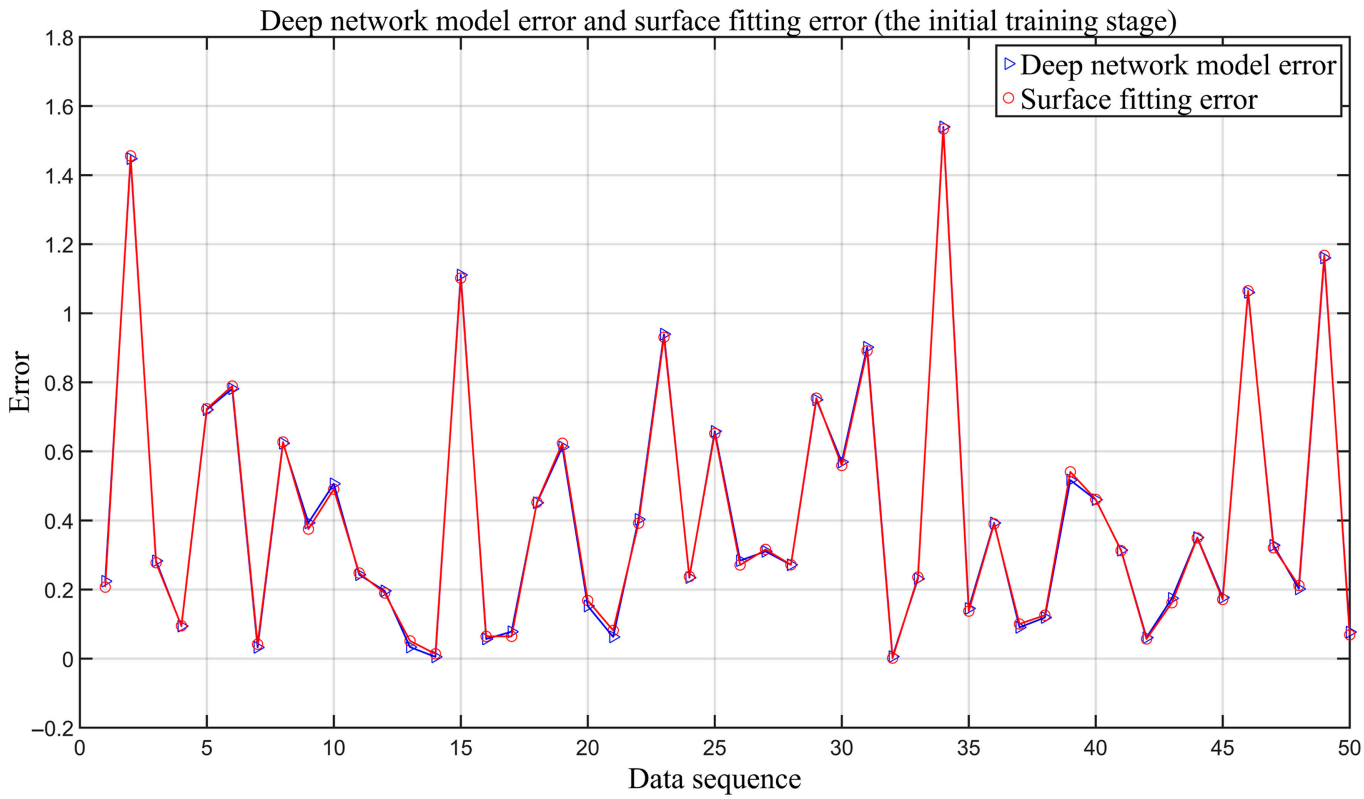

Fig. 14. Deep network model error and surface fitting error in the initial stage.

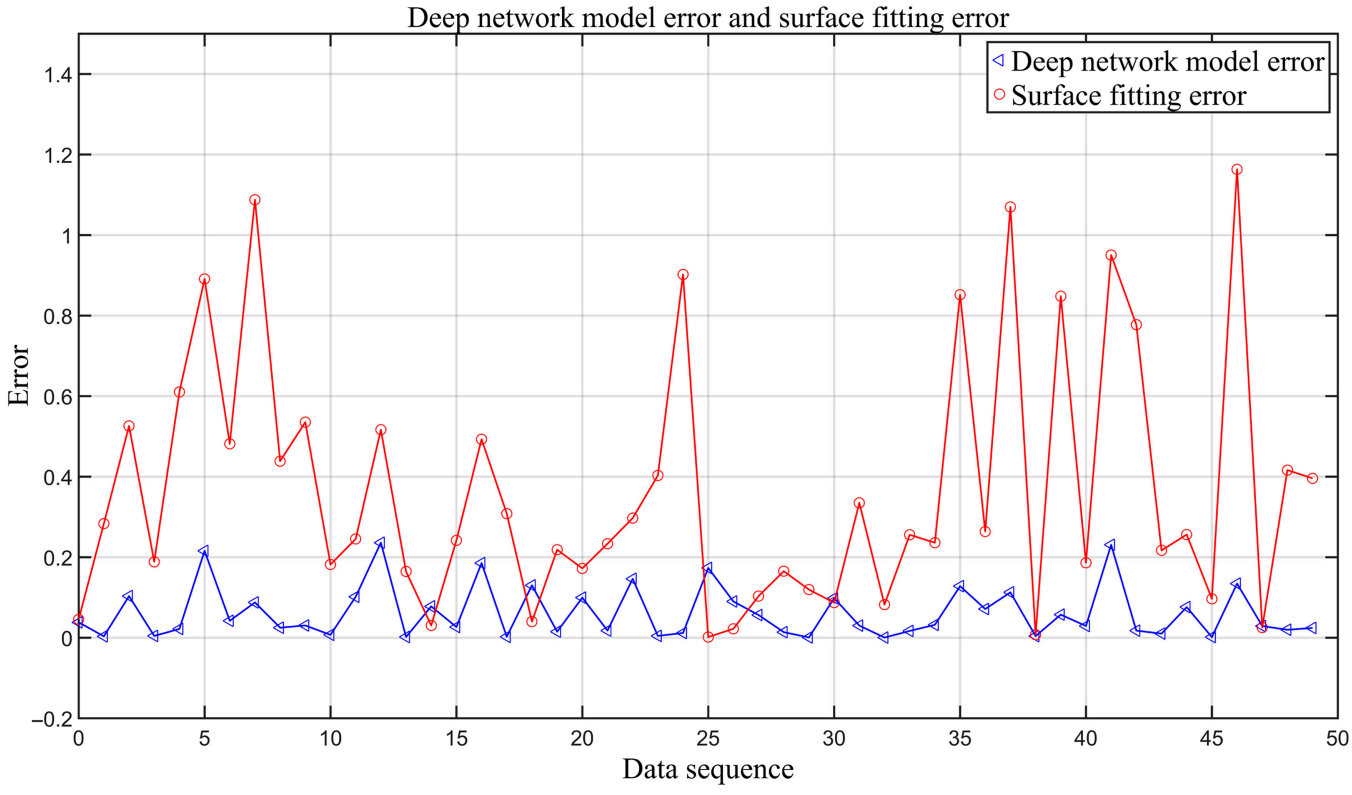

Fig. 15. Deep network model error and surface fitting error.

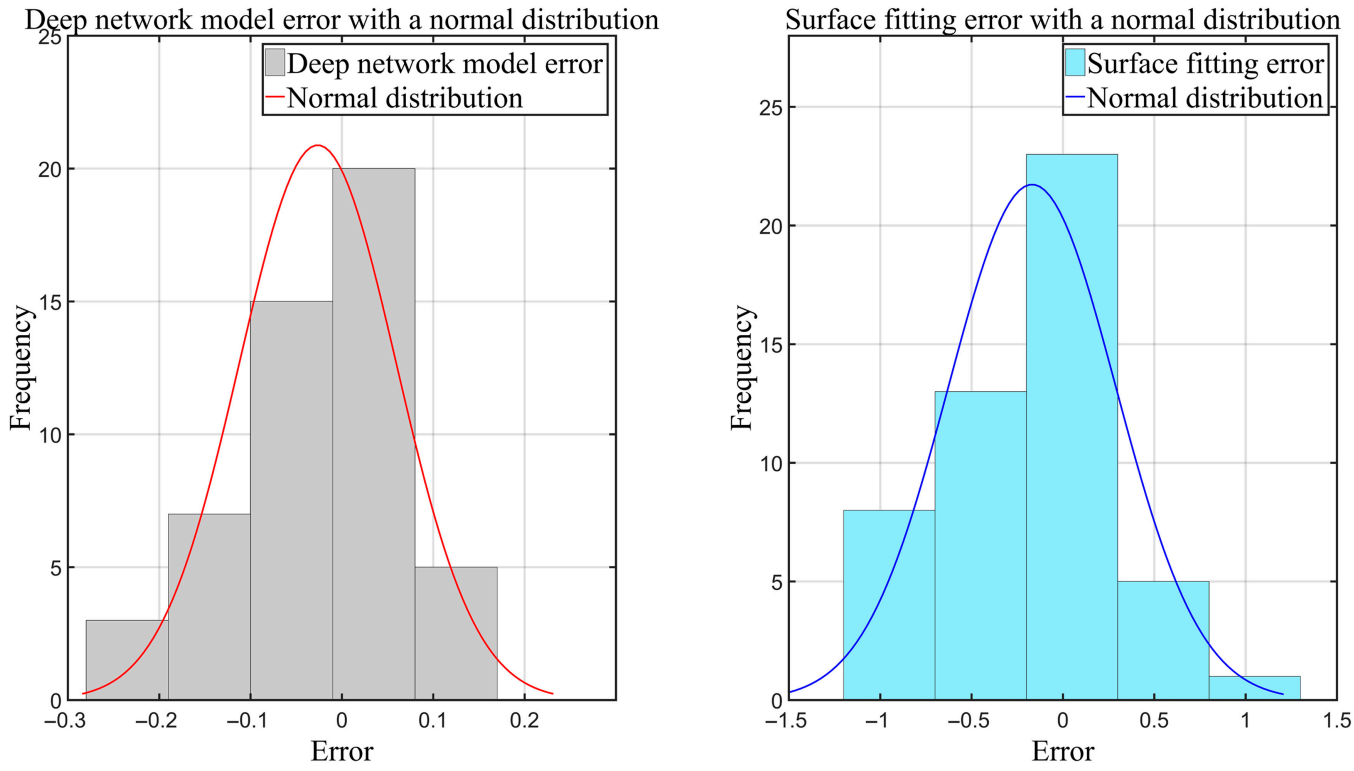

Fig. 16. The errors with a normal distribution.

network. The notation N denotes the number of samples that are randomly chosen from the training dataset in each training iteration. The Adam algorithm is employed to minimize the MSE.

Model optimizing

In general, the training process of the neural network can be roughly divided in 2 stages. In the first stage, the predicted value is calculated by each network node. In the second stage, the backpropagation algorithm is used to calculate the gradient of the loss function for each parameter.

Gradient-based optimization can be used to optimize the value of a function. For example, ω is the input parameter of the function and $L(\omega)$ is the function that needs to be optimized, and gradient-based optimization means defining ω to minimize $L(\omega)$. The gradient descent method varies ω along the negative direction of the gradient of the function to obtain a smaller $L(\omega)$. The function that needs to be minimized is the target function. In the calibration and correction network of the sun sensor, ω generally refers to the parameters in the neural network, and $L(\omega)$ represents the loss function on the training dataset. The general idea of using gradient descent optimization networks is to find a parameter ω that minimizes the loss function $L(\omega)$.

$\frac{\partial}{\partial\omega}L(\omega)$ is the gradient of the function $L(\omega)$ with respect to the parameter ω. In addition, a learning rate (σ) is needed to define the magnitude of each update. The update formula can be obtained as follows:

$$\omega_{n+1} = \omega_n - \sigma \cdot \frac{\partial}{\partial\omega}L(\omega) \tag{15}$$

The gradient descent algorithm optimizes the value of a single parameter, while the backpropagation algorithm is a scheme that efficiently uses the gradient descent algorithm on all parameters. The backpropagation algorithm propagates the information of the loss function backward through the network to calculate the gradient [25]. The Adam algorithm (proposed by Kingma and Ba in 2014 [26]) is a learning rate-adaptive optimization algorithm further improved based on the RMSProp algorithm. First, it assumes a global learning rate σ, and exponential decay rates of moment estimation are ρ_1 and ρ_2 (the value range is [0,1)). Then, it initializes the parameter ω as a small constant δ (default value $\delta = 10^{-8}$) created for numerical robustness. The first-order moment and second-order moment variables s and r, with initial values of 0, as well as the time count t, repeat the following steps until the stop condition is met [26].

Step 1: A small batch of data containing m samples was taken from the training dataset $\{X_1, X_2, X_3, \cdots X_m\}$. The target corresponding to the data is represented by $\hat{\lambda}_i$.

Step 2: The gradient was calculated according to the following formula based on small-batch data:

$$g \leftarrow \frac{1}{m}\nabla_\omega \sum_i L\left(\mathrm{Net}\left(X_i;\omega\right),\hat{\lambda}_i\right)$$

Step 3: Update:

$$t \leftarrow t + 1$$

Step 4: Update the first-order biased moment estimation:

$$s \leftarrow \rho_1 \cdot s + \left(1 - \rho_1\right) \cdot g$$

Step 5: Update the second-order biased estimator, $\otimes$ means multiplying elements of the same coordinate:

$$r \leftarrow \rho_2 \cdot s + \left(1 - \rho_2\right) \cdot g \otimes g$$

Step 6: Correct the deviation of the first moment:

$$\hat{s} \leftarrow \frac{s}{1-{\rho_1}^t}$$

Step 7: Correct the deviation of the second moment:

$$\hat{r} \leftarrow \frac{r}{1-{\rho_2}^t}$$

Step 8: Calculate the number of parameter updates:

$$\Delta\omega = -\sigma\frac{\hat{s}}{\sqrt{\hat{r}+\delta}}$$

Step 9: Update parameters according to $\Delta\omega$:

$$\omega \leftarrow \omega + \Delta\omega$$

Results and Discussion

This section introduces how the deep network model can be created for the calibration experiment of a simulated sun sensor. The calibration experiment of simulated sun sensor based on deep learning includes 3 parts: feedforward neural network construction, neural network training, and neural network fitting test. After analyzing the model, the structure of the feedforward neural network can be determined according to the characteristics of the data. The computer CPU is an i7-12700F 4.9 GHz and the RAM is 32 GB, and the computer GPU is an RTX3060 and the RAM is 12GB.

Data preprocessing

A deep neural network model needs a dataset for training and learning. However, it is difficult to get enough data because it takes a considerable time to obtain experimental data in the calibration experiment of the sun sensor. This dataset limitation may lead to the phenomenon of non-convergence or overfitting of network model training. Therefore, the training of the network model is divided into 2 stages. In the initial training stage, the dataset is generated by the cubic surface fitting model (instead of using experimental data). The deep neural network model uses this dataset for learning and training. When the loss function of the network model converges to the minimum region, it indicates that the learning of the initial training of the network is completed. In the final training stage, the deep network model adopts the measured data for learning. Although the scale of measured data is small, the network parameters at this time are close to the actual model, so it is easy to converge in the training process.

Considering that the FOV range of the analog sun sensor is 60°, the incidence angle ranges from 0° to 60°, and the azimuth angle ranges from −180° to 180°. The dataset generated by the cubic surface fitting model contains 40,000 sets of data. Then, training data should be randomly divided into a training set and a testing set. The proportions of these sets can be adjusted for specific problems. In this work, the proportions are set to 80% and 20%, respectively.

Before deep neural network training, learning data should be normalized. The data normalization process is to convert all data into data between 0 and 1, which is to eliminate the order of magnitude difference of data of various dimensions and avoid large network prediction errors caused by a large order of magnitude difference in input data. The data normalization method in this paper is the max–min method.

$$\overline{X}_k = \frac{X_k - X_{\min}}{X_{\max} - X_{\min}} \tag{16}$$

X_k is a set of input data, and k is the serial number of the datum. $X_{\max}$ and $X_{\min}$ are the maximum and minimum values of corresponding data. The value range of incidence and azimuth is (0°,60°) and (-180°,180°), respectively.

Model training

The modeling of analog sun sensor calibration algorithm based on deep learning includes 3 parts: feedforward neural network construction, neural network training, and neural network fitting test. The flow chart of the algorithm is shown in Fig. 10. After analyzing the model, the structure of the feedforward neural network can be determined according to the characteristics of the data. Table 2 shows the structural parameters of feedforward neural network.

Figure 11 shows the schematic diagram of model training and testing. In the initial training stage of the feedforward neural network model, the dataset is constructed by the least cubic surface fitting model. The learning rate parameter is set to 0.01, batch size to 1,000, and epochs to 100.

Figure 12 shows the loss training curves for the training dataset (blue) and the test dataset (red). The training time is about 52 min (3,120 s). With the increase in training times, the loss training converges to a fixed area with an approximate value of 3.1×10^{-5}. The test set curve fluctuates near the blue line during each process, indicating that the deep network has good generalization performance.

After network learning in the initial stage, the error between the output of the network model and the estimated value of the cubic surface fitting model is concentrated within 0.02°, indicating that the deep network model at this time can better map the cubic surface fitting model. Figure 13 shows the error of deep network calibration and cubic surface fitting result.

To test the training effect of the initial stage, 50 groups of test data were randomly selected and input into the deep network model and surface fitting model for prediction. The results are compared with the theoretical incident angle. Figure 14 shows the errors of the 2 prediction models. After the initial training of the network model, the model parameters have converged to the "optimal value." Therefore, the measured dataset is used to further adjust and correct the network parameters. The measured dataset contains 900 sets of data. In the final stage of the feedforward neural network model, the dataset is collected using an experimental equipment. The learning rate parameter is set to 0.00001 and the batch size to 100.

To test the training effect of the final stage, 50 groups of test data were randomly selected and input into the deep network model and cubic surface fitting model for prediction. Figure 15 shows the errors of the 2 calibration models. From the experimental results, the prediction effect of the deep network model is significantly better than that of the surface fitting model, which indicates that the training is effective. As shown in Fig. 16, after the correction training with the experimental dataset, the calibration error of the incident angle can reach 0.1° (1σ) and 0.25° (3σ), which greatly improves the calibration effect of the cubic surface fitting model. Meanwhile, the error distribution is relatively uniform. Even near the edge of the FOV, there is no large

error. This shows that the method can effectively eliminate deterministic errors, including spot distortion and assembly errors.

Conclusion

The error sources of the 4-quadrant analog sun sensor include assembly error, light spot distortion, and signal characteristics of electronic devices, which make the calibration of the sun sensor cumbersome and limit the accuracy. In this paper, by establishing a deep neural network, a fitting of the error model is conducted, using preliminary and correction training. The incident angle accuracy of the sun sensor is 1° (1σ) before correction, while after applying the neural network model, the accuracy is improved to 0.1° (1σ). Moreover, the error compensation model can eliminate the distortion of the light spot at the edge of the FOV, improving the accuracy, which provides a favorable condition for the FOV expansion of the 4-quadrant analog sun sensor. There are some open points for improvement in this paper. First, the method used is a data-driven method based on deep learning. To achieve error elimination, each sun sensor requires "data collection," "cubic surface fitting," and "deep model training." In general, large datasets facilitate deep model learning. However, the size of experimental datasets on a sun sensor is limited, due to the huge cost of experiment time. In this case, increasing the depth of the model to improve the accuracy may lead to "overfitting." Therefore, the limited data scale brings a negative influence on the further improvement of sun sensor accuracy. In this paper, the deep model training stage is divided into "initial training" and "final training," which is an attempt aimed at overcoming the limited data. The validation experiment proves the effectiveness of this method. In future studies, more ideas and methods will be explored to break through the problems brought by limited data.

Acknowledgments

Funding: The authors would like to express their acknowledgment of the support provided by the National Key Research and Development Program of China (project no. 2021YFE0116000) and the Open Research of State Key Laboratory of Structural Analysis for Industrial Equipment (project no. GZ20103). **Author contributions:** X.-Z.Y. conceived the idea of this manuscript. Q.-B.S. performed the data sampling and the data analysis and deep model learning experiment. J.L.R.G. joined the research of the sun sensor during his internship in China. X.-Z.Y. guided the data sampling, data analysis, and writing of the manuscript. All authors discussed the results and contributed to the final version of the manuscript. **Competing interests:** All authors declare that there is no conflict of interest related to this paper or its publication.

Data Availability

The data used to support the findings of this study are available from the corresponding author upon request.

References

1. Antonello A, Olivieri L, Francesconi A. Development of a low-cost sun sensor for nanosatellites. *Acta Astronautica*. 2018;144:429–436.
2. Wei M, Xing F, You Z, Wang G. Multiplexing image detector method for digital sun sensors with arc-second class accuracy and large FOV. *Opt Express*. 2014;22(19):23094–23107.
3. Wang J, Wang H, Ying P, Jin Z. Design of four quadrant analog sun sensor. *Chin J Sens Actuators*. 2012;25(12):1659–1663.
4. Chen F, Feng J. Analogue sun sensor based on the optical nonlinear compensation measuring principle. *Meas Sci Technol*. 2007;18(7):2111.
5. Qiao-yun F, Guang-jun Z, Xin-guo W. Sun sensor calibration based on exact modeling with intrinsic and extrinsic parameters. *J Beijing Univ Aeronaut Astronaut*. 2011;37(10):1293–1297.
6. Han K, Jin Z-h, Wang H. Optimal attitude determination method for pico-satellite using solar panels. *J Zhejiang Univ Eng Sci*. 2010;44(9):1719–1723.
7. Walker A, Kumar M. CubeSat attitude determination using low-cost sensors and magnetic field time derivative. Paper presented at: AIAA SciTech 2017. Proceedings of the 55th AIAA Aerospace Sciences Meeting; 2017 Jan 9–13; Grapevine, Texas.
8. Deng S, Meng T, Wang H, Du C, Jin Z. Flexible attitude control design and on-orbit performance of the ZDPS-2 satellite. *Acta Astronaut*. 2017;130:147–161.
9. Jiahe M, Tian L. New kind of self-powered wireless digital sun sensor. Paper presented at: ITOEC 2017. Proceedings of the 2017 IEEE 3rd Information Technology and Mechatronics Engineering Conference; 2017 Oct 3–5; Chongqing, China.
10. Huang X, Li M, Wang X, Hu J, Zhao Y, Guo M, Xu C, Liu W, Wang Y, Hao C, et al. The Tianwen-1 guidance, navigation, and control for Mars entry, descent, and landing. *Space Sci Technol*. 2021;2021:Article 9846185.
11. Zhang L. Development and prospect of Chinese lunar relay communication satellite. *Space Sci Technol*. 2021;2021:Article 3471608.
12. Feng M, Yu X, Bai B, Zhou J, Guo J. Design and realization of low-cost micro wireless automatic sun sensor. *Syst Eng Electron*. 2019;41(8):1852–1857.
13. Yousefian P, Durali M, Rashidian B, Jalali MA. Fabrication, characterization, and error mitigation of non-flat sun sensor. *Sens Actuator A Phys*. 2017;261:243–251.
14. Wang C-Y, Liang H, Zhengxin LV, Sun J, Hong S, Sun Y, Chong H. Analysis of error sources existing in dual-axial analog sun sensor. *Aerosp Control Appl*. 2016;42(1):43–47.
15. Xu X, Wang J, Chong H, Gao C, Liang H, Hong S, Lyu Z, Sun Y, Wang C. Error source analysis and compensation in test chain for dual-axial analog sun sensor. *Chin Space Sci Technol*. 2019;39(1):19–24.
16. Deng H-j, Wang H, Wang B-d, Jin Z-h. High-precision compensation and calibration method for four-quadrant analog sun sensor. *J Zhejiang Univ Eng Sci*. 2021;55(10):1993–2001.
17. Adnane A, Cheriet MEA, Benfriha E, Bellar A, Mohammed MAS, Kebbati Y. Sun sensor design for full field of view coverage. Paper presented at: IC_ASET 2022. Proceedings of the 5th International Conference on Advanced Systems and Emergent Technologies ; 2022 Mar 22–25; Hammamet, Tunisia.
18. Porras Hermoso A, Alfonso Corcuera D, Piqueras J, Roibás-Millán E, Cubas J, Pérez-Álvarez J, Pindado S. Design and calibration process of solar sensors for small satellite missions. Paper presented at: SSEA 2022. Proceedings of the 4th Symposium on Space Educational Activities; 2022 Apr 27–29; Barcelona, Spain.

19. Chu W, Wu S, Wu Z, Wang Y. Least square based ensemble deep learning for inertia tensor identification of combined spacecraft. *Aerosp Sci Technol*. 2020;106:Article 106189.
20. Yang H, Yan J, Li S. Fast computation of the Jovian-moon three-body flyby map based on artificial neural networks. *Acta Astronaut*. 2020;193:710–720.
21. Cheng L, Wang Z, Song Y, Jiang F. Real-time optimal control for irregular asteroid landings using deep neural networks. *Acta Astronaut*. 2020;170:66–79.
22. Cybenko G. Approximation by superpositions of a sigmoidal function. *Anal Theory Appl*. 1993;5(4):17–28.
23. Hornik K, Stinchcombe M, White H. Multilayer feedforward networks are universal approximators. *Neural Netw*. 1989;2(5):359–366.
24. Wu S-F, Steyn WH. Modelling and in-orbit calibration practice of a miniature 2-axis analogue sun sensor. *Aerosp Sci Technol*. 2002;6(6):423–433.
25. Rumelhart DE, Hinton GE, Williams RJ. Learning representations by back-propagating errors. *Nature*. 1986;323:533–536.
26. Kingma D, Ba J. Adam: A method for stochastic optimization. arXiv. 2014. https://doi.org/10.48550/arXiv.1412.6980